Random-field Ising model on isometric lattices: Ground states and non-Porod scattering

Arunkumar Bupathy,[1] Varsha Banerjee,[1] and Sanjay Puri[2]
[1]*Department of Physics, Indian Institute of Technology, Hauz Khas, New Delhi 110016, India*
[2]*School of Physical Sciences, Jawaharlal Nehru University, New Delhi 110067, India*
(Received 26 August 2015; published 7 January 2016)

We use a computationally efficient graph cut method to obtain ground state morphologies of the random-field Ising model (RFIM) on (i) simple cubic (SC), (ii) body-centered cubic (BCC), and (iii) face-centered cubic (FCC) lattices. We determine the critical disorder strength Δ_c at zero temperature with high accuracy. For the SC lattice, our estimate ($\Delta_c = 2.278 \pm 0.002$) is consistent with earlier reports. For the BCC and FCC lattices, $\Delta_c = 3.316 \pm 0.002$ and 5.160 ± 0.002, respectively, which are the most accurate estimates in the literature to date. The small-r behavior of the correlation function exhibits a *cusp regime* characterized by a cusp exponent α signifying fractal interfaces. In the paramagnetic phase, $\alpha = 0.5 \pm 0.01$ for all three lattices. In the ferromagnetic phase, the cusp exponent shows small variations due to the lattice structure. Consequently, the interfacial energy $E_i(L)$ for an interface of size L is significantly different for the three lattices. This has important implications for nonequilibrium properties.

DOI: 10.1103/PhysRevE.93.012104

I. INTRODUCTION

Materials contain intrinsic disorder due to defects, impurities, and strained structures. On the other hand, many important systems, such as alloys, spin glasses, and relaxor ferroelectrics, have materialized due to the introduction of disorder. It plays an important role in the behavior of phases and phase transitions in these systems, and introduces a multitude of time scales leading to slow domain growth, anomalous relaxation, and aging even on macroscopic time scales [1–7]. The random-field Ising model (RFIM) is one of the simplest models that captures the effect of disorder [8,9]. It comprises N Ising spins on a d-dimensional lattice with the Hamiltonian given by

$$\mathcal{H}(\{\sigma_i\}) = -J \sum_{\langle ij \rangle} \sigma_i \sigma_j - \sum_i h_i \sigma_i, \quad \sigma_i = \pm 1. \qquad (1)$$

Here, $J > 0$ is the strength of the interaction between the nearest-neighbor (nn) spins and promotes ferromagnetic order. The random fields h_i introduce disorder and are generally drawn from a Gaussian distribution:

$$P(h_i) = \frac{1}{\sqrt{2\pi\Delta^2}} e^{-h_i^2/(2\Delta^2)}. \qquad (2)$$

The standard deviation Δ is a measure of the strength of disorder. The competition between order and disorder introduces a complex free-energy landscape with deep valleys separated by barriers that grow exponentially with the system size. The system then gets trapped in local minima and is often unable to approach the global minimum (or the ground state) over observation time scales. Consequently, many issues related to the equilibrium and nonequilibrium behavior of the RFIM still remain unanswered even after four decades of intense investigations.

One of the earliest questions about the RFIM was regarding the lower critical dimension d_l above which there exists a stable ferromagnetic phase. Imry and Ma, using simple arguments based on domain-wall stability, predicted $d_l = 2$ [10]. Perturbative renormalization group arguments by Young predicted $d_l = 3$ [11]. However, rigorous proofs by Imbrie [12], Bricmont and Kupiainen [13], and Aizenman and Wehr [14] showed that for low disorder and temperature there exists long-range order in the $d = 3$ RFIM, thus establishing $d_l = 2$. There has also been much debate about the nature of the phase transition in RFIM. The earliest Monte Carlo (MC) simulations due to Young and Nauenberg reported a first-order transition [15], while latter studies involving ground-state calculations reported a second-order transition [16–20]. Further, using the technique of replica symmetry breaking, Mezard *et al.* predicted an intermediate glassy phase separating the ferromagnetic and paramagnetic phases [21,22]. But Middleton and Fisher, via a detailed numerical study, showed that the transition is continuous and that there is no intermediate glassy phase [23].

Queries about universality have also been topical and interesting in the context of RFIM. A large number of numerical works suggested universality violations [24–28]. But recently, Fytas and Martin-Mayor have shown from high-statistics simulations that the universality class of the $d = 3$ RFIM is independent of the form of the implemented random-field distribution and the discrepancies observed earlier are due to scaling corrections [29]. Much work has also been done on finding critical exponents and the scaling relations obeyed by them. Malakis and Fytas [30] used novel MC methods to estimate the specific heat exponent at nonzero temperatures. Their study also revealed violation of self-averaging for the specific heat in the RFIM. The comprehensive numerical studies by Fytas-Martin-Mayor and Picco-Sourlas have yielded the most accurate estimates of critical exponents till date [29,31]. Another significant contribution has been the scaling theory of phase transitions in the RFIM [32–34].

At $T = 0$, all the information about the system is contained in the ground state (GS). According to the *zero-temperature fixed-point hypothesis*, transitions at $T = 0$ and $T \neq 0$ are in the same universality class. Thus, the low-temperature phase of the RFIM is controlled by the $T = 0$ fixed point. It is therefore of great interest to obtain ground states of the RFIM. Fortunately, the max-flow and min-cut techniques or the *graph-cut* methods (GCM) provide the global minimum of the energy function specified by Eq. (1), thereby yielding

exact ground states [35]. Recently, Shrivastav *et al.* analyzed these morphologies, which revealed compact domains of up and down spins separated by rough fractal interfaces [36,37]. Consequently, the structure factor, obtained in small-angle neutron scattering experiments, exhibited a crossover from a *Porod regime* [38,39] at intermediate-k values as a consequence of the smooth domains to a *non-Porod* tail due to the fractal interfaces. These observations are a significant step toward understanding the ubiquity of multiple length scales, plethora of relaxation times, and slow relaxation in systems with quenched disorder [36,37].

The RFIM has been fascinating for experimentalists as well. It is realized by a large number of physical systems.

(i) In 1979, Fishman and Aharony showed that randomly *diluted antiferromagnets* (DAFFs) in a uniform field H applied colinearly with the direction of spontaneous ordering maps directly into the RFIM [40]. Since then, DAFFs have been extensively investigated and ensuing observations interpreted using the RFIM [41–45]. The most commonly studied DAFFs have been the insulating, uniaxial antiferromagnets FeF_2, CoF_2, and MnF_2 diluted with nonmagnetic compounds such as ZnF_2 [41–43]. Stable structures are formed because both sets of compounds have a body-centered tetragonal (bct) rutile structure.

(ii) Recently the diluted dipolar insulating magnet $LiHo_xY_{1-x}F_4$ in the presence of a transverse magnetic field has been proven to be a *ferromagnetic* realization of the RFIM [46,47]. It has a bct structure and exhibits a rich phase diagram due to the interplay of dilution and the field and has the distinction of exhibiting a classical as well as a quantum phase transition. The RFIM is providing a starting point for their understanding.

(iii) A class of technologically important materials are ferroelectric single crystals of $A_xBa_{1-x}Nb_2O_6$ ($A = Sr, Pb$) with tetragonal tungsten-bronze structure and $A(B_1B_2)O_3$ ($B_1 = Mg,Zr$; $B_2 = Nb,Ti$) compositions of lead-based perovskite structures [48–50]. They exhibit a transition from ferroelectric to relaxor behavior characterized by slow relaxation and aging and have been identified as examples of the *ferroic* RFIM.

(iv) Molecular magnet Mn_{12}-acetate [51,52], the hexagonal mixed Ising-XY antiferromagnets $Fe_xCo_{1-x}TiO_3$ and $Fe_xCo_{1-x}Cl_2$ [53,54], the kagome staircase lattice ferromagnet $(Co_{1-x}Mg_x)_3V_2O_8$ [55], and sintered needles of $Nd_2Fe_{14}B$ in a transverse field with a hexagonal structure [56,57] are other examples of the RFIM, but have received less attention.

Besides the above examples, diverse systems such as colloid-polymer mixtures, colossal magnetoresistance oxides, and nonequilibrium phenomena such as the Barkhausen noise in magnetic hysteresis have been studied within the purview of the RFIM.

Although the experimental realizations of the RFIM come on a variety of lattice structures, theoretical studies have generally concentrated on simple cubic (SC) lattices. The major distinction between different lattice types is in the number of nn and their distance from the reference site. *How consequential are these factors for the static and dynamic properties of experimental systems?* A few authors have addressed this question. Very recently Akinci *et al.* used effective mean-field theory to obtain phase diagrams for the RFIM with different random-field distributions on SC, body-centered cubic (BCC), and face-centered cubic (FCC) lattices [58]. They also provided estimates of the critical disorder Δ_c for these lattices. In another work, Koiller *et al.* studied interface properties in the $d = 2$ RFIM on square, triangular, and honeycomb lattices [59]. An important consequence of quenched disorder is pinning and roughening of interfaces. These are characterized by a roughness exponent α and are self-affine with a fractal dimension $d_f = d - \alpha$. Koiller *et al.* observed a transition from faceted to fractal interfaces with increasing disorder. This transition was first order for the honeycomb lattice but second order for the square and triangular lattices.

Interfacial properties are significant in the context of many nonequilibrium phenomena. Let us consider the $d = 3$ RFIM, which exhibits a transition from the ferromagnetic phase ($\Delta < \Delta_c$) to the paramagnetic phase ($\Delta > \Delta_c$). The ferromagnetic phase comprises macroscopic domains of up (down) spins containing impurities of down (up) spins. Most nonequilibrium properties involve the motion of interfaces or domain walls. However, in the RFIM and other disordered systems, this motion is impeded by the presence of impurity barriers. The characteristic time to surmount a barrier of energy E_B is given by $\tau(T) = \tau_0 \exp(E_B/T)$. For the RFIM, Villain argued that $E_B \sim R^m$, where R is the characteristic domain size [32]. He estimated the barrier exponent $m = 2 - \alpha$. The power-law behavior demonstrates the nontrivial dependence of E_B (and thereby τ) on the roughness exponent. A closely related topic of current interest is that of domain wall dynamics on the application of an external driving field. This is important for spintronic devices such as magnetic logic gates, racetrack memories, random-access memories, etc. The much-studied *creep* motion of the driven domain wall prior to the depinning transition is greatly affected by interfacial roughness. Universality classes of materials in experiments are now being identified by evaluating the *creep exponent* [60].

In this paper, we use an efficient graph-cut algorithm due to Boykov and Kolmogorov (BK) [61] to obtain *exact* ground states ($T = 0$) of SC, BCC, and FCC lattices. Its polynomial complexity of $O(N)$ allowed us to obtain comprehensive numerical results from large scale simulations. We investigated these morphologies and obtained the following results:

(i) By evaluating the Binder cumulant, the critical point (Δ_c) at $T = 0$ has been estimated for each of the three lattice types. For the SC lattice, $\Delta_c = 2.278 \pm 0.002$ and is consistent with earlier reports. For the BCC and FCC lattices, $\Delta_c = 3.316 \pm 0.002$ and 5.160 ± 0.002, respectively. These are the most accurate estimates in the literature thus far.

(ii) In the paramagnetic phase, the correlation length $\xi(\Delta) \sim (\Delta - \Delta_c)^{-\nu}$ as $\Delta \to \Delta_c^+$ with $\nu = 1.28 \pm 0.01$ for all the three lattice types.

(iii) In the paramagnetic phase, $C(r,\Delta)$ is characterized by a universal scaling function for different disorder amplitudes and lattice types. It shows a cusp singularity at short distances: $1 - C(r,\Delta) \sim r^\alpha$, where the universal exponent $\alpha = 0.5 \pm 0.01$. The corresponding interfaces are fractal with dimension $d_f = d - \alpha$.

(iv) In the ferromagnetic phase, $C(r,\Delta)$ is again characterized by a universal scaling function for different disorder amplitudes. However, the scaling functions show small variations in the short-distance cusps for the three lattice types.

The interfaces in the ferromagnetic phase are also fractal. The roughness exponents vary between $\alpha = 0.68 \pm 0.01$ for SC and $\alpha = 0.64 \pm 0.01$ for FCC.

(v) The large-k behavior of the structure factor $S(k,\Delta)$ exhibits a *non-Porod* regime if the scattering is by fractal interfaces: $S(k,\Delta) \sim k^{-(d+\alpha)}$. We identify this regime in several experimental realizations of the RFIM by analyzing the structure factor obtained by small-angle neutron scattering experiments.

(vi) Finally, we find that the interfacial energy in the ferromagnetic phase is significantly different in the three lattices despite the small variations in the interfacial roughness. Consequently, growth and relaxation are significantly affected by the lattice structure.

This paper is organized as follows. In Sec. II, we briefly describe the Boykov-Kolmogorov (BK) graph-cut method (GCM) to obtain exact ground states of the RFIM. The tools for morphology characterization, viz., the correlation function and the structure factor, are also described in this section. Section III A presents the evaluation of the critical points and exponents associated with the SC, BCC, and FCC lattices. The ground states of the RFIM on these isometric lattices and their morphological properties are discussed in Sec. III B. The implications of the morphologies in the context of domain growth and relaxation are discussed Sec. III C. Experimental evidences of the distinct non-Porod regimes in the two phases are presented in Sec. III D. Finally, in Sec. IV, we conclude this paper with a summary and discussion.

II. METHODOLOGY

A. Graph-cut method

We describe the graph-cut method (GCM) in brief as the details have been described in our earlier papers [37,62]. Consider a set of sites $\mathcal{S}$, each of which is assigned a label $s_i \in \mathcal{L}$. The energy function defining such an assignment is

$$E(\{s_i\}) = \sum_{\{ij\}\in\mathcal{N}} V_{ij}(s_i,s_j) + \sum_{i\in\mathcal{S}} D_i(s_i). \tag{3}$$

The function D_i is the cost of assigning the label s_i to site i, and $V_{ij}(s_i,s_j)$ is the penalty of assigning labels s_i and s_j to neighboring sites i and j. For the application of the GCM, the energy function to be minimized is represented as a graph $\mathcal{G}$, which is an ordered pair of disjoint sets $(\mathcal{V},\mathcal{E})$, where $\mathcal{V}$ is the set of vertices and $\mathcal{E}$ is the set of edges. An edge ij connecting vertices i and j is given a weight V_{ij}. A partitioning of the vertices $\mathcal{V}$ into two sets $\mathcal{Q}$ and $\mathcal{R}$ is called a cut $\mathcal{C}$. Any edge $ij \in \mathcal{E}$ with $i \in \mathcal{Q}$ and $j \in \mathcal{R}$ (or vice versa) is a cut edge. The cost of the cut is the sum of the weights of the cut edges. The problem is to find the cut with the smallest cost or the min-cut. The resulting labeling also minimizes the energy function.

In the case of binary labels, i.e., $\mathcal{L} = \{0,1\}$, the energy function is graph representable if it satisfies the regularity condition [35]:

$$V_{ij}(0,0) + V_{ij}(1,1) \leqslant V_{ij}(0,1) + V_{ij}(1,0). \tag{4}$$

Additionally, if the energy function is quadratic, then the graph-cut is guaranteed to give the global minimum of the energy. It can be immediately seen that by defining $s_i = (1+\sigma_i)/2$, the Hamiltonian of Eq. (1) satisfies regularity. Hence, by mapping the RFIM to a min-cut problem, exact ground states can be obtained in polynomial time. There are many algorithms for finding the min-cut with different polynomial time complexities [63,64]. We have made use of the BK method, which is known to be faster than others due to its polynomial time complexity of $O(N)$ [61].

B. Correlation function and structure factor

A powerful probe for quantifying domain morphologies is the correlation function [65],

$$C(\vec{r},\Delta) = \langle\sigma_i\sigma_j\rangle - \langle\sigma_i\rangle\langle\sigma_j\rangle, \tag{5}$$

where $\vec{r} = \vec{r}_j - \vec{r}_i$ and the angular brackets denote an ensemble averaging. Scattering experiments measure the structure factor, which is the Fourier transform of the correlation function:

$$S(\vec{k},\Delta) = \int d\vec{r} e^{i\vec{k}.\vec{r}} C(\vec{r},\Delta), \tag{6}$$

where $\vec{k}$ is the wave vector of the scattered beam. In the isotropic case, $C(\vec{r},\Delta)$ and $S(\vec{k},\Delta)$ depend on the vector magnitudes $r = |\vec{r}|$ and $k = |\vec{k}|$, respectively. If the system is characterized by a single length scale, the morphology of the domains does not change with Δ, apart from a scale factor. In this case, the correlation function and the structure factor exhibit a scaling property: $C(r,\Delta) = g(r/\xi)$ and $S(k,\Delta) = \xi^d f(k\xi)$. The characteristic length scale $\xi(\Delta)$ is defined from the correlation function as the distance over which it decays to (say) half its maximum value.

A typical GS morphology for the RFIM comprises correlated regions or domains of up and down spins separated by rough interfaces. Consider a domain of size ξ with interfacial width w, which will be defined below. (There is also the microscopic length a denoting the underlying lattice spacing.) For such a morphology, the correlation function is well approximated as [36,37,62]

$$\bar{C}(r) \equiv 1 - C(r) \simeq Ar^\alpha + Br + \cdots. \tag{7}$$

The first term conveys information about the interfacial texture, which can be probed by length scales $a \ll r \ll w$. In this regime, $C(r)$ exhibits a cusp singularity characterized by the roughness exponent α and is a consequence of rough interfaces separating phases. They are generally described as self-affine fractals with a dimension $d_f = d - \alpha$. The linear decay in Eq. (7) dominates at $w \ll r \ll \xi$. It is characteristic of scattering from smooth morphologies in inhomogeneous systems and is termed the *Porod law* [39,66].

Often, the surface roughness is described using the *solid-on-solid* model [67,68]. In this model, the surface is described by a single-valued function $h(\vec{r})$, which represents the height of the surface at a position vector $\vec{r}$ on a $(d-1)$-dimensional substrate. The *interface width* is the root mean square fluctuation in the height:

$$w^2 = \frac{1}{A}\int d\vec{r}[h(\vec{r}) - \bar{h}]^2 = \frac{1}{A}\int d\vec{r}\delta h(\vec{r})^2, \tag{8}$$

where $A = L^{d-1}$ is the substrate area and $\bar{h}$ is the average height. For a translationally invariant system, we can also write

$$w^2 = \langle h(\vec{r})^2\rangle - \langle h(\vec{r})\rangle^2, \tag{9}$$

where the angular brackets denote an ensemble average: $\langle h(\vec{r})\rangle = \bar{h}$. We expect $w^2 \sim L^{2\alpha}$, where α is the roughness exponent of the interface [67]. Once again, for a self-affine surface, $d_f = d - \alpha$. We stress that the correlation-function data yields a more accurate measure of α, as it is obtained by averaging over all interfaces in the system.

The short-distance cusp singularity has important implications for the structure factor $S(k)$. It decays with an asymptotic power-law form [69–72]:

$$S(k) \sim \tilde{A}(\xi k)^{-(d+\alpha)} + \tilde{B}(\xi k)^{-(d+1)}. \tag{10}$$

The dominant large-k behavior in Eq. (10) is the *cusp regime* $S(k) \sim (\xi k)^{-(d+\alpha)}$, with crossover to the *Porod decay* characterized by $S(k) \sim (\xi k)^{-(d+1)}$ at intermediate wave-vectors.

III. NUMERICAL RESULTS

The ground states of the RFIM on SC, BCC, and FCC lattices were obtained using the BK GCM on lattices of size L^3 ($L \leqslant 160$), with periodic boundary conditions in all directions. We have chosen $J = 1$, so all energies are in units of J. Unless specified otherwise, the data presented here is for a system of size $L = 160$. Note that the SC lattice has only one spin per unit cell, whereas the BCC and FCC lattices have two and four spins per unit cell, respectively. Thus, for a system of size L, the SC lattice has L^3 spins, BCC lattice has $2L^3$ spins and FCC lattice has $4L^3$ spins. The initial condition was chosen to be a random mix of $\sigma = \pm 1$. Our studies indicate that the BK GCM yields states with a 99% overlap with the GS in the first iteration itself, provided the disorder strength is not too close to the critical value Δ_c. All the results have been averaged over at least 100 sets of $\{h_i\}$ for each value of Δ and sometimes even more to improve the quality of our numerical data. For calculating the correlation function $C(r,\Delta)$ of the BCC and FCC lattices, extra sites with $\sigma_i = 0$ have been introduced, thereby converting them to SC lattices with lattice spacing $a/2$. With this, the structure factor $S(k,\Delta)$ could be obtained with ease using standard fast Fourier transform routines. These data have been spherically averaged *only* over those vector lengths, which are physically relevant for the particular lattice in consideration.

A. Critical points and exponents

First, we determine the the critical disorder strength Δ_c, below which the cubic lattices exhibit ferromagnetic long-range order. These values are expected to depend on the number of nn, which are 6, 8, and 12 for the SC, BCC, and FCC lattices, respectively. One of the most efficient procedures to determine the critical point uses the fourth-order Binder cumulant, defined as [73–75]

$$U_4 = 1 - \frac{\langle m^4\rangle}{3\langle m^2\rangle^2}, \tag{11}$$

where m is the average magnetization of the system. A plot of U_4 versus Δ for different lattice sizes L intersects at the critical point. For the SC lattice, we had estimated $\Delta_c = 2.278 \pm 0.002$ in an earlier paper and refrain from reproducing the corresponding plot of U_4 vs. Δ here [62]. In Fig. 1 we show the evaluation of U_4 versus Δ for (a) + (c) BCC lattice with

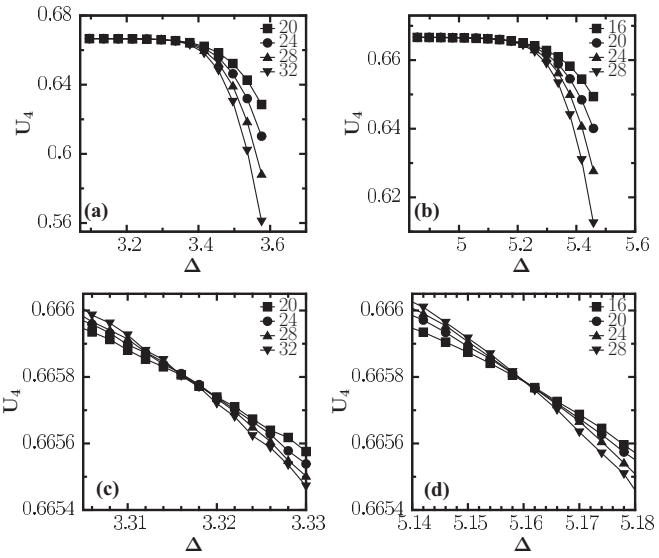

FIG. 1. Binder cumulant U_4 plotted as a function of Δ for (a)+(c) BCC lattice and (b)+(d) FCC lattice for different lattice sizes L. $\Delta_c = 3.316 \pm 0.002$ for the BCC lattice and $\Delta_c = 5.160 \pm 0.002$ for the FCC lattice. The lower frames show a zoomed-in view of the data.

$L = 20, 24, 28$, and 32; and (b) + (d) FCC lattice with $L = 16$, 20, 24, and 28. The data have been averaged over as many as a million realizations in some cases to obtain the point of intersection of lines corresponding to U_4 versus Δ. We have provided the statistics in Table I. We obtain (a) $\Delta_c = 3.316 \pm 0.002$ for the BCC lattice and (b) $\Delta_c = 5.160 \pm 0.002$ for the FCC lattice. To the best of our knowledge, these values are the most accurate in the literature thus far. Recently, Akinci *et al.* obtained Δ_c to be 3.8501 (SC), 5.450 (BCC), and 8.601 (FCC) using an effective-field approximation [58]. These values are grossly different from our evaluations made using *exact* GS morphologies.

As the disorder strength is decreased from $\Delta = \infty$, correlated regions or domains of size ξ rich in either up or down spins start forming. Defining $\delta = (\Delta - \Delta_c)/\Delta_c$, we depict typical GS morphologies of the three lattices in Fig. 2. The upper frames correspond to $\delta = 0.08$ (paramagnetic state), and the lower frames correspond to $\delta = -0.01$ (ferromagnetic state). Green and blue regions represent up and down spins, respectively. The unit cell in each case is depicted in the corner of the upper frames for reference. As can be observed, the correlation length $\xi \to \infty$ as $\delta \to 0^+$, the divergence

TABLE I. Simulation parameters for the evaluation of Binder cumulants. L is the lattice size and N_r is the number of disorder realizations.

BCC		FCC	
L	N_r	L	N_r
20	6×10^6	16	4×10^6
24	2×10^6	20	1×10^6
28	1×10^6	24	6×10^5
32	6×10^5	28	4×10^5

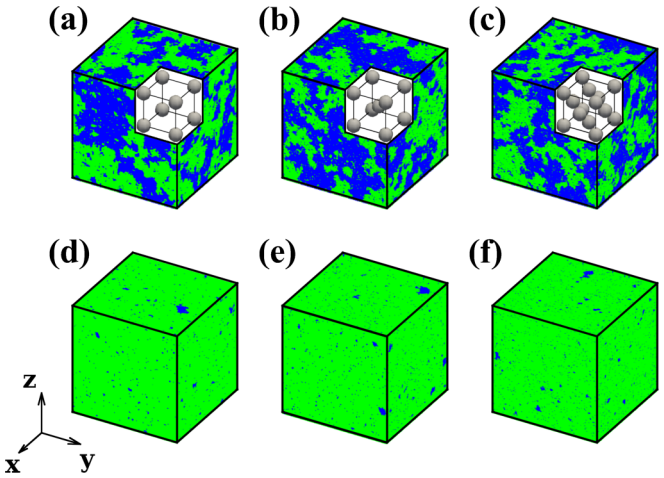

FIG. 2. Ground-state morphologies of the RFIM on cubic lattices of size 160^3. (a), (b), and (c) are typical ground-state configurations of the SC, BCC, and FCC lattices for $\delta = (\Delta - \Delta_c)/\Delta_c = 0.08$. Green (gray) and blue (black) regions represent up and down spins, respectively. The corresponding unit cells are shown in the insets. (d), (e), and (f) represent typical ground-state configurations of the SC, BCC, and FCC lattices for $\delta = -0.01$.

limited by lattice size L. To investigate finite-size effects, we plot $\xi(\delta, L)$ versus δ for the paramagnetic phase in Fig. 3(a) for system sizes L ranging from 64 to 160 obtained for SC, BCC, and FCC lattices. The finite-size scaling ansatz $\xi(\Delta) = \delta^{-\nu} F(L\delta^{\nu})$ for $\nu = 1.28 \pm 0.01$ yield the master curves depicted in Fig. 3(b). The same value of ν for all the three lattice structures suggests that the nn environment is inconsequential in the paramagnetic phase. We believe that this result is generic, and that the correlation length exponent ν is universal for all lattice types in the paramagnetic phase. This is consistent with our expectation that the microscopic details of the lattice are not relevant near criticality.

B. Morphological properties

Next, we do a detailed investigation of the GS morphologies of the RFIM on the three lattices in the paramagnetic phase.

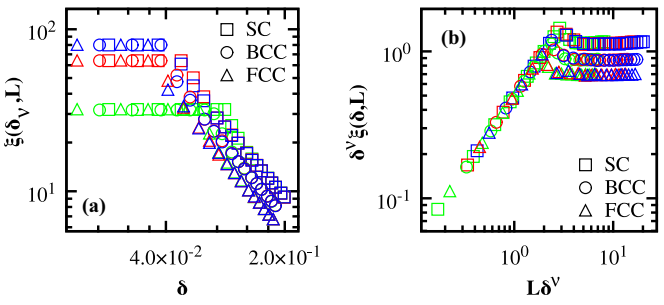

FIG. 3. Log-log plot of $\xi(\delta, L)$ vs. δ in the paramagnetic phase (with $\delta > 0$) for different system sizes L. The denoted symbols represent SC, BCC, and FCC lattices respectively, and the different colors (shades) denote different L. The direct plot is shown in (a), whereas (b) shows data collapse resulting from the finite-size scaling ansatz $\xi(\Delta) = \delta^{-\nu} F(L\delta^{\nu})$ with $\nu = 1.28 \pm 0.01$ for all the three lattices.

The top row in Fig. 4 shows typical slices [in the (xy) plane] of the GS morphologies of the (a) SC, (b) BCC, and (c) FCC lattices, respectively, for $\delta = 0.08$. The enclosed portion in the square is magnified to clearly identify the arrangement of sites in each lattice type. It should be noted that the nn are at a distance a for SC, $\sqrt{3}a/2$ for BCC, and $a/\sqrt{2}$ for FCC. While the nn for the SC and FCC slice lie in the same plane, those for the BCC slice lie in adjacent planes at a distance $a/2$.

We quantify the textures of domains and interfaces by evaluating the correlation function $C(r, \Delta)$ and the structure factor $S(k, \Delta)$. For each lattice, the scaled correlation functions for different disorder amplitudes with $\delta > 0$ are numerically indistinguishable (not shown here). Figure 4(d) depicts the scaled correlation function, $C(r, \Delta)$ versus r/ξ, for disorder strength $\delta = 0.08$ for SC, BCC, and FCC lattices. The collapse is excellent, indicating that in the paramagnetic phase the correlation function is scale-invariant with respect to disorder and the lattice type as well. Figure 4(e) shows the log-log plot of $1 - C(r, \Delta)$ versus r/ξ yielding a cusp exponent $\alpha = 0.5 \pm 0.01$. This implies that the interfaces separating the up-spin and down-spin regions in the paramagnetic phase have a fractal dimension of $d_f \simeq 2.5$. The corresponding scaled structure factor, $\langle k \rangle^3 S(k, \Delta)$ versus $k/\langle k \rangle$ on a log-log scale, is plotted in Fig. 4(f). The solid line denotes a non-Porod regime with slope -3.5. We believe that in the paramagnetic phase, the cusp exponent $\alpha = 0.5$ is universal and does not depend on the details of the lattice structure.

Let us next look at the ferromagnetic phase for $\Delta < \Delta_c$. The corresponding morphology consists of a macroscopic up (down) phase with impurity islands of down (up) spins—see lower frames of Fig. 2. To set up interfaces, we consider a $d = 3$ cubic lattice of size L^3 (with $L = 128$). A single interface is set up perpendicular to the z direction by fixing the spin values at $z = 1, L$:

$$\begin{aligned} \sigma(x, y, z = 1) &= -1, \\ \sigma(x, y, z = L) &= +1. \end{aligned} \tag{12}$$

Periodic boundary conditions are deployed in the (x, y) directions. For a particular field realization $\{h_i\}$, the GCM is then implemented to obtain the ground state subject to the above boundary condition. The top row in Fig. 5 shows vertical cross-sections of the 3-d snapshots at $x = L/2$ for (a) SC lattice, (b) BCC lattice, and (c) FCC lattice. These morphologies have been obtained for $\delta = -0.01$. Figures 5(d)–5(f) show the corresponding (xy) cross-sections at $z = \bar{h}$, the average height of the interface.

To study morphological differences in the ferromagnetic phase, we calculate the correlation functions $C(r, \Delta)$ for different values of $\Delta < \Delta_c$. The correlation function is evaluated only in the (xy) plane at $z = \bar{h}$ since the system is not translationally invariant in the z direction. For a given lattice, the scaled correlation functions for different disorder amplitudes are numerically indistinguishable. For brevity, we do not show these results here. Figure 5(g) depicts the scaled correlation function, $C(r, \Delta)$ versus r/ξ, for disorder strength $\delta = -0.1$. The three data sets correspond to the different lattices. The scaling for small values of r/ξ is not as clean as in Fig. 4(d) corresponding to the paramagnetic phase. To probe the interfacial properties, we plot $1 - C(r, \Delta)$ versus r/ξ

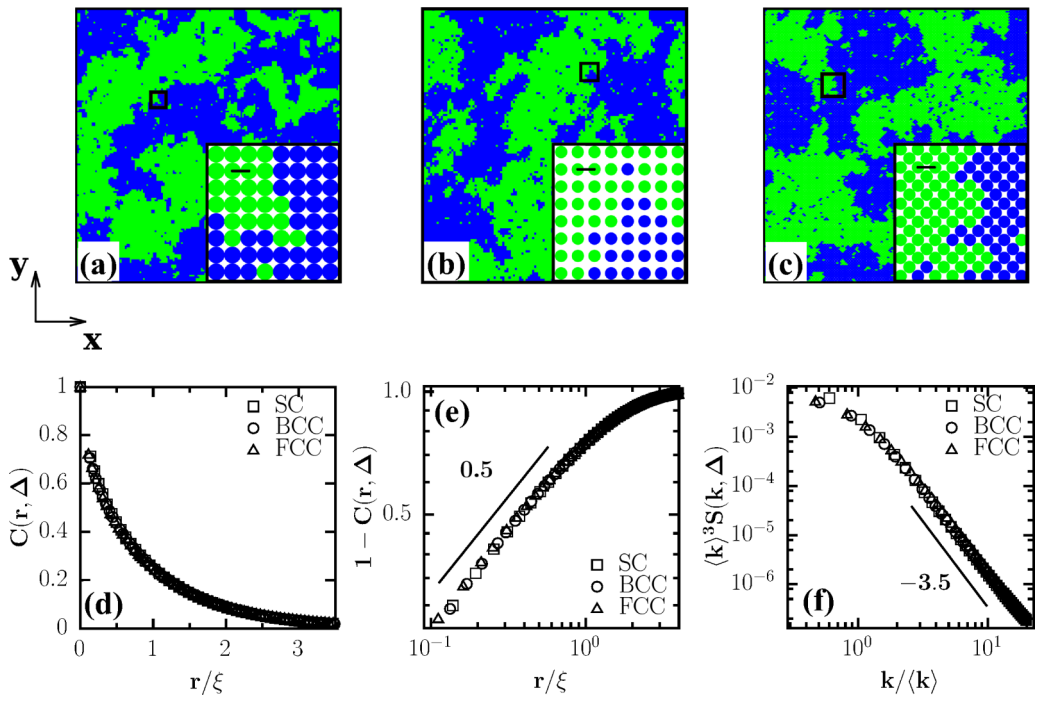

FIG. 4. Typical slices (at $z = L/2$) of the ground-state morphologies of the RFIM in the paramagnetic phase ($\delta = 0.08$) on (a) SC, (b) BCC, and (c) FCC lattices. Green (gray) and blue (black) regions represent up and down spins, respectively. The region enclosed by the small black square is shown magnified in the inset. The black line in the inset represents the length of one unit cell a. The scaled correlation function, $C(r,\Delta)$ vs. r/ξ, for disorder strength $\delta = 0.08$ is shown in (d). The specified symbols denote SC, BCC, and FCC lattices, respectively. The log-log plot of $1 - C(r,\Delta)$ vs. r/ξ is shown in (e). The cusp exponent $\alpha = 0.5 \pm 0.01$ for all three lattices. The corresponding log-log plot of the scaled structure factor, $\langle k\rangle^3 S(k,\Delta)$ vs. $k/\langle k\rangle$, is shown in (f). The solid line in (f) denotes a non-Porod regime with slope -3.5.

in Fig. 5(h). The data reveals a cusp regime for all three lattices with cusp exponents in the range $\alpha \approx 0.64$–0.68. These minor differences may be attributed to the different structures of the underlying lattices.

C. Energy barriers to relaxation

Under what circumstances can the cusp exponents be consequential? These exponents play an important role in a range of nonequilibrium applications, e.g., the domain growth of the RFIM after a quench from the disordered phase ($\Delta > \Delta_c$) to the ordered phase ($\Delta < \Delta_c$) [7,76]. Recall that rough fractal interfaces are a result of pinning or trapping due to the quenched disorder. They introduce energy barriers and the domain growth then proceeds by thermally activated barrier-hopping, which is characterized by logarithmic (rather than power-law) growth. It is relevant to ask how these barriers are related to the interfacial properties, e.g., the fractal dimension determined by the cusp exponent in Eq. (7). An important study of nonconserved domain growth in the RFIM is due to Villain [32]. Suppose R is the characteristic size of a domain. The growth of this correlated region is via activation over the energy barriers separating the local minima of the complex energy landscape. These activation energies depend on R. Villain argued that the barriers have a power-law dependence on the domain size, $E_B \sim R^m$. He estimated the barrier exponent to be $m = 2 - \alpha$ with $\alpha = (5 - d)/3$.

Systems undergoing domain growth have been classified by Lai *et al.* (LMV) [78] on the basis of how free-energy barriers to coarsening depend on R. The LMV scheme in nonconserved systems is based on the equation for curvature-driven growth:

$$\frac{dR}{dt} = \frac{c(R,t)}{R}. \tag{13}$$

The basis of classification is the R-dependence of the kinetic coefficient $c(R,t)$. *Class 1* systems, for which $c(R,t)$ is independent of R and remains nonzero as $T \to 0$, do not have energy barriers to coarsening. In general, $R \sim t^{1/2}$ for these systems. *Class 2* consists of systems whose energy barriers are independent of R but have a single barrier height E_B, so that $c(R,t) = c_0 \exp(-E_B/T)$. As a result, $R(t) = (c_0 t/\tau)^{1/2}$, where $\tau(T) = \tau_0 \exp(E_B/T)$ is the characteristic time to surmount the barriers. In systems with quenched disorder in the Hamiltonian, e.g., RFIM, spin glasses, etc., the barriers grow as R^m. In this case $c(R,t) = c_0 \exp(-\epsilon_B R^m/T)$, where ϵ_B is the energy barrier per unit length. The short-time growth is governed by $R(t) \sim t^{1/2}$, which crosses over to a logarithmic growth: $R(t) \sim (T\epsilon_B^{-1})^{1/m}(\ln t)^{1/m}$. The particular case of $m = 1$ corresponds to *Class 3* systems, while $m \neq 1$ corresponds to *Class 4* systems. The roughness exponent therefore plays a major role in domain growth and the small variations introduced by the lattice structure may result in vastly different relaxation time scales.

Motivated by the above arguments, we calculate the interfacial energy E_i for the three lattice types. We expect E_i to be closely related to the barrier energy E_B discussed above. We choose $\Delta < \Delta_c$ since the interfacial textures are distinct in this regime. As before, the interfaces are set up by

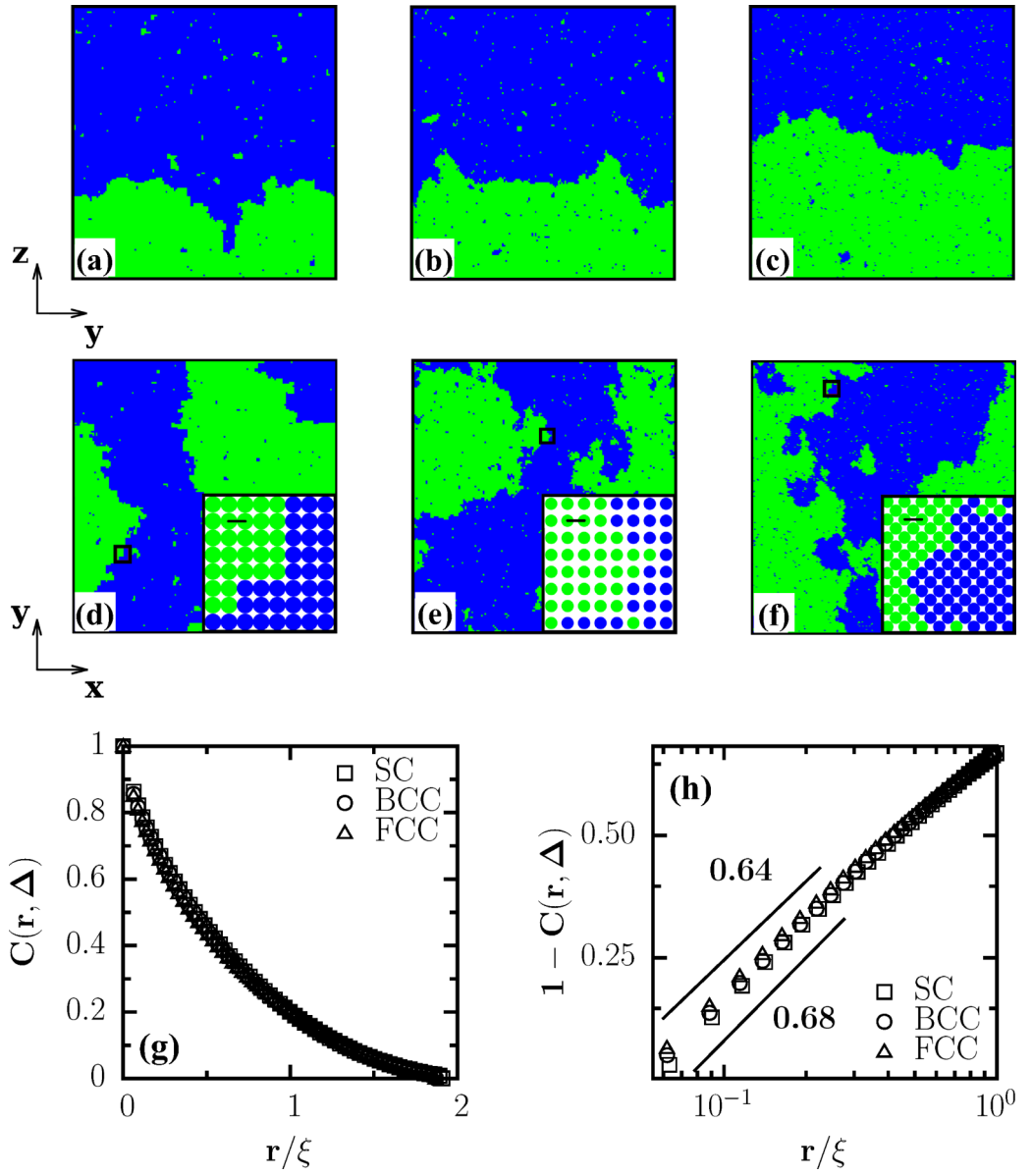

FIG. 5. Vertical slices (at $x = L/2$) of the interfaces in the ferromagnetic phase ($\delta = -0.01$) for (a) SC, (b) BCC, and (c) FCC lattices. Green (gray) and blue (black) regions represent up and down spins, respectively. The corresponding horizontal slices (at $z = \bar{h}$) are shown in (d), (e), and (f). The region enclosed by the small black square is shown magnified in the inset. The black line in the inset represents the length of one unit cell a. The scaled correlation function, $C(r, \Delta)$ vs. r/ξ, for disorder strength $\delta = -0.1$ is shown in (g). The specified symbols denote SC, BCC, and FCC lattices, respectively. The log-log plot of $1 - C(r, \Delta)$ vs. r/ξ is shown in (h). The cusp exponent $\alpha = 0.68 \pm 0.01$ for SC. The cusp exponents for BCC ($\alpha = 0.66 \pm 0.01$) and FCC ($\alpha = 0.64 \pm 0.01$) show minor differences. The corresponding interfaces are fractal with dimension $d_f = d - \alpha$.

imposing antiparallel boundary conditions in the z direction, and periodic boundaries in the x and y directions. On applying the GCM, the resulting interface of lateral size L separates two large domains of up and down spins containing a few small impurities with spins of the opposite kind (see top row of Fig. 5). The latter are removed by making their spin values equal to that of the larger domain enclosing them, thereby creating just a single interface. The interfacial energy $E_i(L)$ is calculated as the difference in energy of this configuration and an all up (down) configuration with the same set of random fields [23,77]. For a given value of L, the results are averaged over 256 field realizations.

In Fig. 6, we plot $E_i(L)$ versus L for SC, BCC, and FCC lattices on a log-log scale. Here, L is in units of the corresponding nn distance and was varied from 8 to 100, and $\delta = -0.1$. Notice that the data for the three lattices are distinct even though the roughness exponents differ only slightly. There is an overall scale factor due to the difference in the coordination numbers of different lattices. However, there is also a slope difference in the small-L regime where the interfacial roughness is relevant. The precise values of the slopes at small-L are difficult to estimate due to the quality of the data. At large-L, there is a crossover to $E_i \sim L^2$, implying that the interfacial roughness is inconsequential on these length

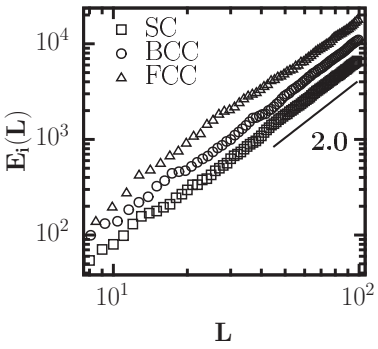

FIG. 6. Plot of the interfacial energy $E_i(L)$ vs. L for $\delta = -0.1$ for the isometric lattices: SC, BCC, and FCC. The solid line with slope 2 mimics the large-L behavior in all the three cases.

scales. To emphasize the significant variation in interfacial energy despite the small variations in the roughness exponents, we provide in Table II the estimates of $E_i(L)$ for $\delta = -0.1$ obtained from our computation.

D. Experimental evidences

The important paper by Fishman and Aharony demonstrated the equivalence of the RFIM and the randomly diluted antiferromagnets (DAFFs) in a uniform field [40]. These systems show novel phenomena due to the presence of multicomponent phases, critical and multicritical points, spin waves, and slow relaxation. Some of the most well-studied DAFFs are $Fe_xZn_{1-x}F_2$ and $Co_xZn_{1-x}F_2$ compounds with a body-centered rutile structure ($a = b \neq c; \alpha = \beta = \gamma = 90$). We analyze their small-angle neutron-scattering data and compare it with our numerical observations in Sec. III B. In Fig. 7 we plot the following data sets on a log-log scale. The critical temperature, the experimental temperature, and the value of the applied magnetic field are also provided in the parentheses for reference:

(1) $Fe_{0.46}Zn_{0.64}F_2$ (32.11 K, 32.34 K, 3.0 T) [79];
(2) $Fe_{0.46}Zn_{0.64}F_2$ (32.11 K, 31.6 K, 3.0 T) [79];
(3) $Co_{0.35}Zn_{0.65}F_2$ (13.25 K, 7 K, 3.5 T) [42];
(4) $Co_{0.35}Zn_{0.65}F_2$ (13.25 K, 2 K, 5.0 T) [42];
(5) $Fe_{0.6}Zn_{0.4}F_2$ (46.13 K, 46.3 K, 2.0 T) [2];
(6) $Fe_{0.76}Zn_{0.24}F_2$ (58.6 K, 20 K, 6.0 T) [80].

The solid line with slope -4 corresponds to the Porod law, which arises from scattering off smooth interfaces. Clearly all data sets are non-Porod with slopes greater than -4, signifying fractal interfaces.

TABLE II. Variation of the interfacial energy $E_i(L)$ with system size L in the ferromagnetic phase for SC, BCC, and FCC lattices at disorder strength $\delta = -0.1$.

	$E_i(L)$		
L	SC	BCC	FCC
8	44.54	86.11	162.98
16	178.17	321.40	608.27
24	400.89	694.41	1314.20
32	712.70	1199.50	2270.10

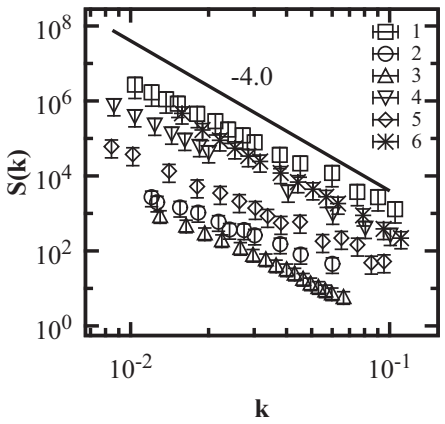

FIG. 7. Log-log plot of neutron scattering data of DAFFs: (1) $Fe_{0.46}Zn_{0.64}F_2$ ($T_c = 32.11$K, $T = 32.34$ K, $H = 3.0$ T) [79]; (2) $Fe_{0.46}Zn_{0.64}F_2$ ($T_c = 32.11$K, $T = 31.6$ K, $H = 3.0$ T) [79]; (3) $Co_{0.35}Zn_{0.65}F_2$ ($T_c = 13.25$ K, $T = 7$ K, $H = 3.5$ T) [42]; (4) $Co_{0.35}Zn_{0.65}F_2$ ($T_c = 13.25$ K, $T = 2$ K, $H = 5.0$ T) [42]; (5) $Fe_{0.6}Zn_{0.4}F_2$ ($T_c = 46.13$ K, $T = 46.3$ K, $H = 2.0$ T) [80]; (6) $Fe_{0.76}Zn_{0.24}F_2$ ($T_c = 58.6$ K, $T = 20$ K, $H = 6.0$ T) [80]. The data sets have been shifted vertically for clarity. The solid line of slope -4 corresponds to Porod scattering from smooth interfaces. It can be clearly seen that the data sets are less steep than the Porod law, signifying fractal interfaces.

We do not expect to detect the small variations in the slopes in the paramagnetic and ferromagnetic phases observed in simulations. They are hard to discern as the accuracy of the scattering data is limited by the resolution function of the detector. Nevertheless, *all* data sets clearly reveal a non-Porod tail, indicating that the interfaces separating phases in DAFFs are *fractal*. Although the experimental realizations of the RFIM appear to have varied lattice forms, corresponding small-angle scattering data has not been recorded. We are therefore unable to interpret the corresponding morphological information in these systems.

IV. SUMMARY AND DISCUSSION

We conclude this paper with a summary of our results. The RFIM is representative of many physical systems with disorder. Such systems possess a complex free-energy landscape with many local minima, which impede the approach to the ground state. They exhibit slow relaxation and a multitude of relaxation times, which are influenced by the underlying lattice structure. In this paper, we have obtained the exact GS of the RFIM on three isometric lattices: SC, BCC, and FCC. Our aim was to understand the role played by the distinct environments created by the position and the number of nn on GS morphologies. We have characterized them using correlation functions $C(r)$ and structure factors $S(k)$, which contain information averaged over all domains and interfaces. Therefore, our numerical results have a high degree of precision. The main results of our paper are as follows.

(a) The critical disorder strengths for the isometric lattices are (i) $\Delta_c = 2.278 \pm 0.002$ for SC, (ii) $\Delta_c = 3.316 \pm 0.002$ for BCC, and (ii) $\Delta_c = 5.160 \pm 0.002$ for FCC. We believe these to be the most accurate estimates in the literature so far.

(b) In the paramagnetic phase, the correlation length $\xi(\Delta) \sim (\Delta - \Delta_c)^{-\nu}$ as $\Delta \to \Delta_c^+$ with $\nu = 1.28 \pm 0.01$, irrespective of the lattice structure.

(c) Interfaces separating domains of up and down spins are fractal in nature. They are characterized by a fractal dimension $d_f = d - \alpha$, where α is the roughness exponent. In the ferromagnetic phase, $\alpha = 0.68 \pm 0.01$ for the SC lattice with small variations for the BCC and FCC lattices. In the paramagnetic phase, $\alpha = 0.5 \pm 0.01$ for all three lattice types.

(d) We compute the interfacial energy $E_i(L)$, which is closely related to the energy barriers for interface motion. These interfacial energies are vastly different for the three lattice structures, although the variation in the roughness exponent is small.

(e) We identify the signature of fractal interfaces in several experimental realizations of the RFIM by analyzing the structure factor obtained from neutron scattering experiments.

The Lai, Mazenko, and Valls formulation emphasizes the role played by α on growth and relaxation in complex systems. Because of the power-law dependence in the RFIM, significant variations in relaxation time scales are introduced by a small change in α. The latter, as we have observed, critically depends on the lattice structure and the strength of disorder. This important issue has been overlooked in RFIM studies, and our work is one of the first to address it. We hope that the methodologies used and results obtained in this work may be beneficial from both theoretical and experimental points of view.

ACKNOWLEDGMENTS

A.B. and V.B. acknowledge financial support from Department of Science and Technology (DST), India and Indo-French Centre for Advanced Scientific Research, India. S.P. acknowledges support from the DST, India through a J.C. Bose fellowship.

[1] R. A. Cowley, H. Yoshizawa, G. Shirane, M. Hagen, and R. J. Birgeneau, Phys. Rev. B **30**, 6650 (1984).
[2] D. P. Belanger, A. R. King, and V. Jaccarino, Phys. Rev. B **31**, 4538 (1985).
[3] D. A. Huse and C. L. Henley, Phys. Rev. Lett. **54**, 2708 (1985).
[4] T. Nattermann and I. Vilfan, Phys. Rev. Lett. **61**, 223 (1988).
[5] P. Lehnen, W. Kleemann, Th. Woike, and R. Pankrath, Phys. Rev. B **64**, 224109 (2001).
[6] S. Puri, Phase Trans. **77**, 469 (2004).
[7] F. Corberi, E. Lippiello, A. Mukherjee, S. Puri, and M. Zannetti, Phys. Rev. E **85**, 021141 (2012).
[8] T. Nattermann and J. Villain, Phase Trans. **11**, 5 (1988).
[9] T. Nattermann, in *Spin Glasses and Random Fields*, edited by A. P. Young (World Scientific, Singapore, 1998).
[10] Y. Imry and S. K. Ma, Phys. Rev. Lett. **35**, 1399 (1975).
[11] A. P. Young, J. Phys. C: Solid State Phys. **10**, L257 (1977).
[12] J. Z. Imbrie, Phys. Rev. Lett **53**, 1747 (1984); Commun. Math. Phys. **98**, 145 (1985).
[13] J. Bricmont and A. Kupiainen, Phys. Rev. Lett. **59**, 1829 (1987).
[14] M. Aizenman and J. Wehr, Phys. Rev. Lett. **62**, 2503 (1989).
[15] A. P. Young and M. Nauenberg, Phys. Rev. Lett. **54**, 2429 (1985).
[16] A. T. Ogielski and D. A. Huse, Phys. Rev. Lett. **56**, 1298 (1986).
[17] H. Rieger and A. P. Young, J. Phys. A **26**, 5279 (1993).
[18] H. Rieger, Phys. Rev. B **52**, 6659 (1995).
[19] M. E. J. Newman and G. T. Barkema, Phys. Rev. E **53**, 393 (1996).
[20] A. T. Ogielski, Phys. Rev. Lett. **57**, 1251 (1986).
[21] M. Mézard and A. P. Young, Europhys. Lett. **18**, 653 (1992).
[22] M. Mézard and R. Monasson, Phys. Rev. B **50**, 7199 (1994).
[23] A. A. Middleton and D. S. Fisher, Phys. Rev. B **65**, 134411 (2002).
[24] J.-C. Anglès d'Auriac and N. Sourlas, Europhys. Lett. **39**, 473 (1997).
[25] M. R. Swift, A. J. Bray, A. Maritan, M. Cieplak, and J. R. Banavar, Europhys. Lett. **38**, 273 (1997).
[26] N. Sourlas, Comput. Phys. Commun. **121–122**, 183 (1999).
[27] A. K. Hartmann and U. Nowak, Eur. Phys. J. B **7**, 105 (1999).
[28] B. Ahrens, J. Xiao, A. K. Hartmann, and H. G. Katzgraber, Phys. Rev. B **88**, 174408 (2013).
[29] N. G. Fytas and V. Martin-Mayor, Phys. Rev. Lett. **110**, 227201 (2013).
[30] A. Malakis and N. G. Fytas, Phys. Rev. E **73**, 016109 (2006).
[31] M. Picco and N. Sourlas J. Stat. Mech. (2014) P03019.
[32] J. Villain, Phys. Rev. Lett. **52**, 1543 (1984).
[33] A. J. Bray and M. A. Moore, J. Phys. C **18**, L927 (1985).
[34] D. S. Fisher, Phys. Rev. Lett. **56**, 416 (1986).
[35] V. Kolmogorov and R. Zabih, IEEE Trans. PAMI **26**, 147 (2004).
[36] G. P. Shrivastav, V. Banerjee, and S. Puri, Eur. Phys. J. E **37**, 98 (2014).
[37] G. P. Shrivastav, M. Kumar, V. Banerjee, and S. Puri, Phys. Rev. E **90**, 032140 (2014).
[38] G. Porod, Kolloid-Z **124**, 83 (1951).
[39] G. Porod, in *Small-Angle X-ray Scattering*, edited by O. Glatter and O. Kratky (Academic Press, New York, 1982).
[40] S. Fishman and A. Aharony, J. Phys. C: Solid State Phys. **12**, L729 (1979).
[41] R. J. Birgeneau, H. Yoshizawa, R. A. Cowley, G. Shirane, and H. Ikeda, Phys. Rev. B **28**, 1438 (1983).
[42] M. Hagen, R. A. Cowley, S. K. Satija, H. Yoshizawa, G. Shirane, R. J. Birgeneau, and H. J. Guggenheim, Phys. Rev. B **28**, 2602 (1983).
[43] J. P. Hill, Q. Feng, R. J. Birgeneau, and T. R. Thurston, Z. Phys. B **92**, 285 (1993).
[44] Q. Feng, R. J. Birgeneau, and J. P. Hill, Phys. Rev. B **51**, 15188 (1995).
[45] F. Ye, L. Zhou, S. Larochelle, L. Lu, D. P. Belanger, M. Greven, and D. Lederman, Phys. Rev. Lett. **89**, 157202 (2002).
[46] S. M. A. Tabei, M. J. P. Gingras, Y.-J. Kao, P. Stasiak, and J.-Y. Fortin, Phys. Rev. Lett. **97**, 237203 (2006).
[47] M. Schechter, Phys. Rev. B **77**, 020401 (2008).
[48] W. Kleemann, J. Dec, P. Lehnen, R. Blinc, B. Zalar, and R. Pankrath, Europhys. Lett. **57**, 14 (2002).
[49] S. Miga, W. Kleemann, J. Dec, and T. Łukasiewicz, Phys. Rev. B **80**, 220103 (2009).

[50] V. Westphal, W. Kleemann, and M. D. Glinchuk, Phys. Rev. Lett. **68**, 847 (1992).
[51] B. Wen, P. Subedi, L. Bo, Y. Yeshurun, M. P. Sarachik, A. D. Kent, A. J. Millis, C. Lampropoulos, and G. Christou, Phys. Rev. B **82**, 014406 (2010).
[52] A. J. Millis, A. D. Kent, M. P. Sarachik, and Y. Yeshurun, Phys. Rev. B **81**, 024423 (2010).
[53] Po-zen Wong, Phys. Rev. B **34**, 1864 (1986).
[54] Q. J. Harris, Q. Feng, Y. S. Lee, R. J. Birgeneau, and A. Ito, Phys. Rev. Lett. **78**, 346 (1997).
[55] K. Fritsch, Z. Yamani, S. Chang, Y. Qiu, J. R. D. Copley, M. Ramazanoglu, H. A. Dabkowska, and B. D. Gaulin, Phys. Rev. B **86**, 174421 (2012).
[56] S. L. Tomarken, D. M. Silevitch, G. Aeppli, B. A. Brinkman, J. Xu, K. A. Dahmen, and T. F. Rosenbaum, Adv. Funct. Mater. **24**, 2986 (2014).
[57] J. Xu, D. M. Silevitch, K. A. Dahmen, and T. F. Rosenbaum, Phys. Rev. B **92**, 024424 (2015).
[58] Ü. Akinci, Y. Yüksel, and H. Polat, Phys. Rev. E **83**, 061103 (2011).
[59] B. Koiller, H. Ji, and M. O. Robbins, Phys. Rev. B **46**, 5258 (1992).
[60] R. H. Dong, B. Zheng, and N. J. Zhou, Europhys. Lett. **98**, 36002 (2012).
[61] Y. Boykov and V. Kolmogorov, IEEE Trans. PAMI **26**, 1124 (2004).
[62] G. P. Shrivastav, S. Krishnamoorthy, V. Banerjee, and S. Puri, Europhys. Lett. **96**, 36003 (2011).
[63] L. Ford and D. Fulkerson, *Flows in Networks* (Princeton University Press, Princeton, 1962).
[64] A. V. Goldberg and R. E. Tarjan, J. ACM **35**, 921 (1988).
[65] S. Puri, in *Kinetics of Phase Transitions*, edited by S. Puri and V. K. Wadhawan (Taylor and Francis, Boca Raton, 2009).
[66] Y. Oono and S. Puri, Mod. Phys. Lett. B **2**, 861 (1988).
[67] A. L. Barabasi and H. E. Stanley, *Fractal Concepts in Surface Growth* (Cambridge University Press, Cambridge, 1995).
[68] P. Meakin, P. Ramanlal, L. M. Sander, and R. C. Ball, Phys. Rev. A **34**, 5091 (1986).
[69] H. D. Bale and P. W. Schmidt, Phys. Rev. Lett. **53**, 596 (1984).
[70] P.-Z. Wong, Phys. Rev. B **32**, 7417 (1985).
[71] P.-Z. Wong and A. J. Bray, Phys. Rev. Lett. **60**, 1344 (1988).
[72] P.-Z. Wong and A. J. Bray, Phys. Rev. B **37**, 7751 (1988).
[73] K. Binder, Z. Phys. B **43**, 119 (1981).
[74] K. Binder and D. W. Heermann, *Monte Carlo Simulation in Statistical Physics: An Introduction, Fourth Edition* (Springer-Verlag, Berlin, 2002).
[75] M. E. J. Newman and G. T. Barkema, *Monte Carlo Methods in Statistical Physics* (Oxford University Press, Oxford, 1999).
[76] S. Puri and N. Parekh, J. Phys. A **26**, 2777 (1993).
[77] K. K. Mon, Phys. Rev. Lett. **60**, 2749 (1988).
[78] Z. W. Lai, G. F. Mazenko, and O. T. Valls, Phys. Rev. B **37**, 9481 (1988).
[79] D. P. Belanger, V. Jaccarino, A. R. King, and R. M. Nicklow, Phys. Rev. Lett. **59**, 930 (1987).
[80] W. C. Barber, F. Ye, D. P. Belanger, and J. A. Fernandez-Baca, Phys. Rev. B **69**, 024409 (2004).